


Article

Fabrication, Wear, and Corrosion Resistance of HVOF Sprayed WC-12Co on ZE41 Magnesium Alloy

Sonia García-Rodríguez *, Antonio Julio López , Victoria Bonache, Belén Torres and Joaquín Rams

Department de Matemática Aplicada, Ciencia e Ingeniería de Materiales y Tecnología Electrónica, ESCET, Universidad Rey Juan Carlos. C/ Tulipán s/n, Móstoles, 28933 Madrid, Spain; antoniojulio.lopez@urjc.es (A.J.L.); victoria.bonache@urjc.es (V.B.); belen.torres@urjc.es (B.T.); joaquin.rams@urjc.es (J.R.)

* Correspondence: sonia.garcia@urjc.es

Received: 7 May 2020; Accepted: 21 May 2020; Published: 24 May 2020



Abstract: This study shows that WC-12Co coatings with low porosity and high wear and corrosion resistance can be applied by high velocity oxygen-fuel (HVOF) on a low melting and highly flammable ZE41 magnesium alloy. This provides a novel and promising use of the high-energy thermal spraying technique on low temperature melting substrates. The spraying distance used was 300 mm, which is between two and three times the recommended distance for HVOF coating with WC-12Co on steels. Despite this, the WC-12Co coatings obtained were homogeneous, crack-free, and dense. The coatings were very well adhered to the substrates and the spraying distance allowed avoiding any thermal affectation of the substrate. The thickness of the coatings was limited to 45 μm to avoid a big mass increase in the samples. The effect of the number of layers, the O_2/H_2 ratio and the gas transport flow in the coating was studied. The coatings reduced the wear rate of the substrate by 104 times, making them wear resistant. Electrochemical corrosion tests were conducted to study the corrosion protection of the coatings, showing that it is possible to protect the magnesium substrate for 96 h in contact with 3.5 wt.% NaCl aqueous solution.

Keywords: magnesium alloy; tungsten carbide; coating; thermal spray; corrosion; wear

1. Introduction

Magnesium and its alloys are increasingly being used in the automotive field because they are the lightest structural metallic materials and have excellent specific strength. The use of these materials could lead to a significant reduction in the weight of vehicles and, therefore, a reduction in fuel consumption. Their ability to dampen vibrations and noise, their dimensional stability, their impact resistance, and their good electrical and thermal conductivity, make them suitable for structural applications [1,2]. However, the use of magnesium alloys in the transport industry is currently limited by its main drawbacks, associated with its surface properties, which are its limited resistance to corrosion and wear [3]. Therefore, the expansion of the field of application of magnesium in the industries depends on the development of new technologies that minimize these disadvantages.

Surface modification is one of the approaches to improve the surface properties of the materials. In this way, many technologies have been applied on the magnesium alloys surface to achieve an improvement in their behavior against corrosion and wear: anodizing [4,5], chemical conversion treatments [6], thermal spray coatings [7], sol-gel coatings [8], or even laser treatments [9] have been studied. Among the different techniques, the use of coatings is the most effective way to improve the surface properties of magnesium alloys. For corrosion protection, different coatings have been applied: organic coatings [10], TiN, TiCN, ZrCN, metallic oxides, Al, Zn, Cr, and Cu coatings [11,12]. Electric-explosive spraying (EES) technique was also used to manufacture coatings that ensures the

formation of pore-free coatings and high adhesion to the base [13]. Electric erosion stable coatings such as W-Cu, W-Cu-Cu, Mo-Cu, Mo-C-Cu, and Ti-B-Cu were developed using this EES technique [14]. Coatings made by thermal spraying processes are receiving the most attention because these techniques allow obtaining coatings that can be used in many different environments, as they have low degree of porosity and high adhesion strength to the substrate, providing protection against corrosion and wear [15–17]. Aluminum, its alloys, and composites have been deposited on magnesium alloys by cold spray [18–20], flame spray [21], or high velocity oxygen fuel (HVOF) [7,22]. The HVOF technique provides coatings with a lower degree of porosity, with values less than 1%, with greater hardness, better adhesion resistance, and higher density than when using other techniques. This is due to the high speed of the sprayed particles and to the particles being sprayed in a molten or semi-molten state. Therefore, these coatings are the best ones for corrosion protection as the other spraying techniques give rise to coatings with more porosity [23]. However, the high energy provided by the flame and the molten or semi-molten particles has traditionally limited the use of HVOF on low melting temperature such as Mg or Al alloys, and is very critical on highly flammable materials such as pure Mg and most Mg alloys.

Stainless steel coatings have been successfully applied on Mg substrates despite the high melting point of the coating material, but the ductility of stainless steel particles allowed obtaining low porosity coating [24]. Protection against corrosion and wear have been obtained on Mg alloys using HVOF stainless steel coatings [25,26]. However, harder materials are available as coatings. The wear and corrosion behavior of the coatings depends not only on the spraying process used, but also on the powder feedstock characteristics and on the microstructure of the manufactured coating [27]. Cermet coatings, such as WC-Co, WC-Co-Cr, and Cr₃C₂-NiCr, produced by different thermal spraying processes (APS, VPS, and HVOF) can be used under different wear conditions such as abrasion, adhesion, fretting, or erosion [28–31]. The use of WC-based coatings manufactured by HVOF has increased in several areas because of its high erosion and erosion-corrosion resistance [32,33]. HVOF of WC-Co results in less decomposition of the WC during spraying process than with other techniques, providing coatings with high density and excellent cohesive strength [34,35]. However, the standard spray conditions of WC-Co involve a high energy density that is incompatible with the melting temperature and flammability of Mg alloys [36].

Therefore, the main objective of this article was to investigate the HVOF spraying conditions that allow to deposit a high melting point WC-Co coating on a commercial magnesium-zinc alloy (ZE41) without damaging the substrate, with the aim to provide new application possibilities for the HVOF technique on substrates that have low melting points. A detailed study of the influence of the main spraying parameters in the characteristics of the coating, i.e., coating thickness, porosity, and composition has been carried out. With the aim to obtain a good barrier for magnesium alloys against wear and corrosion, the corrosion and wear behavior of the different manufactured coatings was analyzed.

2. Materials and Methods

2.1. Materials

Extruded rods of ZE41 cast alloy used as substrate were supplied by Magnesium Elektron Company with a nominal composition (wt.%) of: 4.09 Zn; 1.7 rare earths (Pr + Nd + La + Ce); 0.68 Zr, 0.6 O; and balance Mg. The material was received with the aging treatment T5 (2 h at 330 °C followed by 10–16 h at 177 °C). The rod was cut in 60 mm diameter and 10 mm thick discs and used as substrates. All samples were sand blasted with 1 mm corundum particles, ultrasonically cleaned in ethanol and air-dried before conducting spraying. This process supposes the obtention of a roughness of the magnesium surface of $7.4 \pm 0.4 \mu\text{m}$.

WC-12 wt.% Co powder provided by Oerlikon (Diamalloy 2004, Pfäffikon, Switzerland) was used as feedstock. This powder is mainly used in industry to create dense and well-bonded coatings on

steels for applications against abrasive, fretting wear and erosion, the particle size distribution of the WC-12Co powder was $-45 + 5 \mu\text{m}$ and its nominal composition was (wt.%): 11.5–13.0 Co, 5.25 max. C, 1.5 max. Fe, 1.0 max. others and balance W.

2.2. Spraying Process

WC-12Co coatings were deposited on ZE41 magnesium alloy substrates by high velocity oxygen-fuel (HVOF) using a thermal spraying equipment from Sulzer Metco (Unicoat, DJ2600, Oerlikon Metco, Pfäffikon, Switzerland). The gun was placed on an anthropomorphic robot (ABB IRB-2400/16) to control some of the spraying parameters (spraying distance, gun speed, and number of deposited layers). The different spraying parameters used to manufacture the coatings are shown in Table 1. Oxygen was used as oxidizing gas, hydrogen as fuel gas, and nitrogen was used as transport gas to feed the feedstock powder in the gun. Dry air was used as shielding gas (344 NLPM) and with a feeding rate of 3 g/s. All coatings were sprayed at a distance of 300 mm and using a spraying gun speed of 250 mm/s. This distance and speed were optimized at the first steps of this work and were selected because they allow having a minimum effect on the magnesium substrate. Also, the number of layers deposited was kept low to limit the weight of the coatings.

Table 1. Spraying parameters used in the high velocity oxygen-fuel (HVOF) process.

Parameter	Samples				
	1L-1	2L-1	2L-2	2L-3	2L-4
Layers	1	2	2	2	2
O ₂ /H ₂ ratio	0.34	0.34	0.34	0.31	0.21
Transport gas N ₂ (NLPM)	12.5	12.5	30	30	30

Two O₂/H₂ ratios were used to control the oxidizing effect of the flame and to control the energy provided by the HVOF process. To evaluate the effect of the gas transport flow on the morphology of the different coating, two different values have been used.

2.3. Specimen Examination

For microscopic characterization, metallographic samples were cut using a SiC disc cutter, hot mounted in conductive resin, roughing with SiC emery papers up to 4000 grade and polished with diamond paste up to 1 μm . The morphological and microstructural features of the WC-12Co coatings were analyzed in the cross-section by scanning electron microscopy (SEM, Hitachi S-3400N, Hitachi High-Technologies, Tokyo, Japan), using secondary (SE) and backscattered electron (BSE) imaging, and equipped with an energy dispersive X-ray spectrometer (EDS, XFlash 5010, Bruker, Germany, Europe).

Thickness and porosity content were determined using a light microscope (Leica DMR) with Leica Image-Pro Plus software (version 7.0).

To identify the different phases in the sprayed coatings, all coatings were characterized by X-ray diffraction measurements (DRX, Panalytical, Malvern, UK) using X'Pert PRO apparatus with the CuK α radiation at low angle (1°).

Surface roughness measurements of the coatings were obtained using a 3D optical profiler (Zeta Instruments, Zeta-20, San Jose, CA, USA). Three images were obtained for each specimen, each one with an area of 2.4 mm², to obtain average values.

The coating adhesion strength was evaluated by means of a Posi-Test AT-Pull-Off Adhesion Tester (Defelsko, Ogdensburg, NY, USA), following the ASTM D4541-02 procedure E [37] at a loading rate of 1.0 MPa·s⁻¹ and using 10 mm aluminum dollies, which were glued to the coating using an epoxy adhesive Loctite® EA 9466 Hysol® (Henkel Ibérica S.A, Barcelona, Spain).

Microhardness values across the coatings were measured on the cross-section using a SIHMADZU HMV-2 microhardness tester (Shimadzu Corporation, Kyoto, Japan) following UNE-EN ISO 6507-1 standard [38] using an indentation load of 100 gf ($HV_{0.1}$) and 15 s as residence time. At least 10 hardness tests were conducted on the cross-section of each sample at specific distances to the coating/substrate interface to obtain representative average values.

2.4. Tribological Test

Tribological tests were carried out at room temperature on the substrate and on the different sprayed coatings using a Microtest tribometer (model Microtest MT/10/SCM, Microtest S.A., Madrid, Spain) under dry sliding conditions with a ball-on-disc configuration. In a first attempt, a hard carbon steel-bearing ball with a diameter of 6 mm was used as counterpart. The high wear suffered by this steel counterpart against the two-layer WC-12Co revealed the need of using a harder counterpart. Therefore, a WC-6%Co sintered ball with a diameter of 6 mm from RGP Balls was finally used as the counterpart, using a new ball for each test. The hardness of the counterpart was in the range 1550–1780 HV.

Specimen and counterbody surfaces were cleaned with ethanol before the wear test to avoid the presence of humidity and non-desirable films as grease on them. Wear tests were carried out under load of 10 N and sliding velocity of 1.3 m/s for a total sliding distance of 5000 m. The wear-testing machine records continuously both the distance and the friction coefficient. Samples were weighted before and after the wear test to determine the mass loss during the test. Wear volume loss was determined from the mass loss using the material density to determine the wear rate using the Archard's law [14].

$$\frac{V}{L} = K \frac{W}{H} = kW \quad (1)$$

In this equation V is the wear volume, L is the sliding distance, being the coefficient V/L the wear rate, W is the applied load, H is the hardness of the sample, K is the Archard's constant, and k is the specific wear rate.

2.5. Corrosion Test

Corrosion behavior of the different specimens was evaluated at room temperature using immersion test in a 3.5 wt.% NaCl solution with an Autolab PGStat302N potentiostat (Metrohm, Herisau, Switzerland), provided with Nova 2.1 software. Measurements were carried out using a conventional three-electrode cell configuration using the specimen as the working electrode, a silver/silver chloride (Ag/AgCl) as the reference electrode and a graphite rod as the counter electrode. An area of 0.76 cm² of the samples was exposed to the electrolyte using an aperture in the electrochemical cell, sealed with an O-ring to avoid liquid leakage.

The polarization resistance of the samples (R_p) was obtained by lineal polarization tests varying the potential from ± 10 mV around the corrosion potential (E_{corr}) with a scanning rate of 1 mV/s. These R_p values were obtained for each sample after different immersion times in the electrolyte solution (1, 6, 24, 48, 72, 96, and 168 h) to study the evolution of the coating protection with time. Anodic–cathodic polarization measurements (Tafel curves) were carried out by polarizing between -400 and 800 mV around the corrosion potential with a scanning rate of 1 mV/s and after 1 h of immersion time to allow the stabilization of the open circuit potential (OCP).

3. Results and Discussion

3.1. Powder and Spraying Characterization

The feedstock WC-12Co powder had a polyhedral morphology (Figure 1a) and each powder particle consisted itself in a WC–Co cermet, this structure is characteristic of crushed particles. Small ceramic particles of WC are immersed in a Co matrix, so the ceramic phase constitutes about 80 vol.%

of particles. This can be observed in the SEM micrograph (Figure 1b) where the geometric elements observed in light color correspond to the WC particles (marked by arrows in Figure 1b) and the dark areas correspond to the cobalt matrix. Purity of the feedstock was confirmed using X-ray diffraction pattern where WC and Co peaks were the only ones detected. A wide distribution of particle size was observed by SEM, and 90% of the particle had sizes in the 5–45 μm range. Although the size is smaller than usual for HVOF, it is required because of the high density of this material.

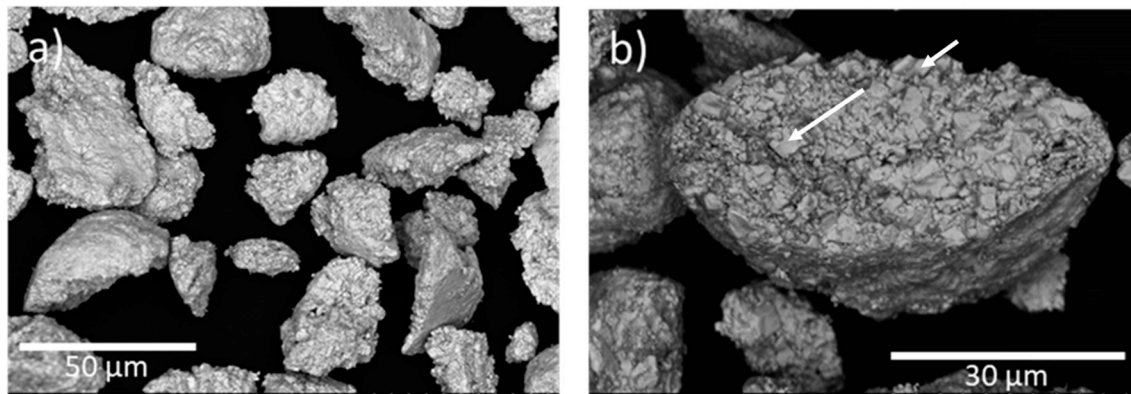


Figure 1. Scanning electron microscopy (SEM) micrographs in the backscattering electron mode of the WC-12Co powder used as feedstock: (a) general view (b) detailed of a particle using higher magnifications.

The spraying conditions used have been changed from the standard ones in order to reduce the heat input to the magnesium substrates in order to avoid its burning or melting and even to cause any heat degradation caused by the HVOF flame. To evaluate the validity of the heat supplied to the cermet particles, a wipe test was carried out using 300 mm of spraying distance and a transversal speed of 1300 mm/s. The high transversal speed of the gun allows the observation of the individual droplets. The SEM observation of the sprayed powder (Figure 2) revealed two different behaviors: (i) The as-received powder lost their initial polyhedral geometry because the molten Co matrix reaches the Mg alloy in a molten state and splashes over it forming individual splats (Figure 2a), (ii) some splash splat with little fingers were observed (Figure 2b,c), suggesting that the molten cobalt matrix reached the substrate with some plastic deformation capacity because of the thermal and kinetic energy obtained from the flame. Therefore, the heat supplied to the particles is enough to melt the metallic phase and allow its deformation upon impacting on the substrate, but the high content of WC particles, which remained solid during the spraying, partially limited the deformation of the particle. The small number of pores observed could be partially filled by the other particles sprayed during coating manufacturing, but some may still remain after it.

On the other hand, the wipe test allows determining the effect of the HVOF sprayed particles on the surface of the substrate used. With this technique, the high linear momentum of the particles, which is the result of the combination of a dense material with a high flight speed of the particles, caused a significant deformation of the ZE41 substrate surface (marked by arrows in Figure 3a,b). As Figure 3 shows, some of the sprayed WC did not adhere to the substrate but caused an increase of the roughness of the substrate. The deformation caused by the sprayed particles was greater than on other substrates such as steel [39] because of the low hardness of the magnesium substrate used. In this case, the use of a large spraying distance did not reduce the speed of the particles because they were still in the HVOF flame, but the heat supplied to the substrate was effectively reduced.

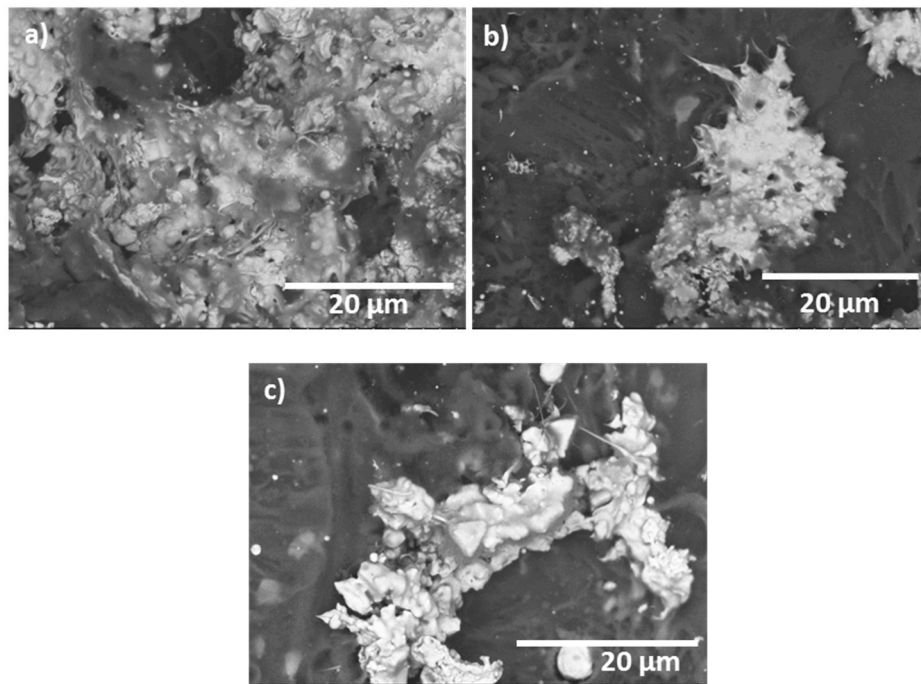


Figure 2. SEM micrographs in the backscattering electron mode of individual sprayed particles of the feedstock powder obtained from the wipe test. (a) Particle deformed after impact, (b) and (c) splash splat with little fingers.

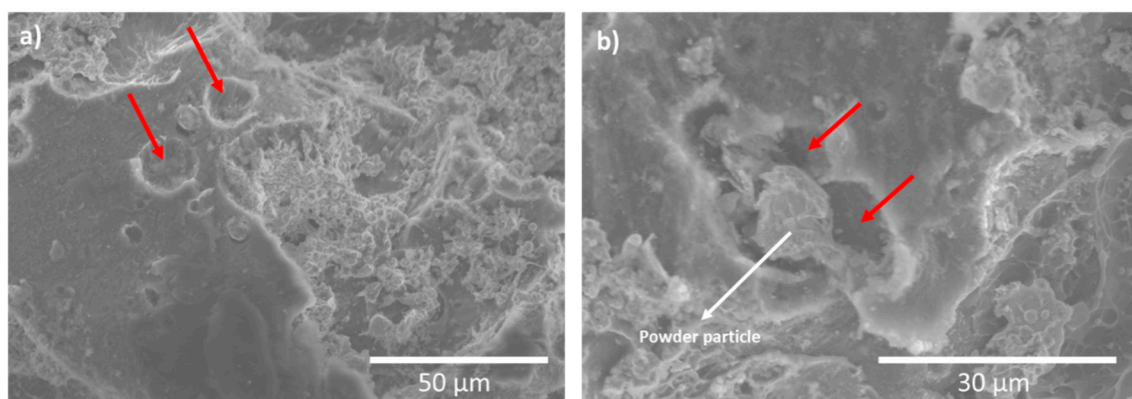


Figure 3. (a) and (b) SEM-micrographs of HVOF sprayed WC-Co particles on ZE41 magnesium alloy.

3.2. Coatings Characterization

The coatings deposited on the ZE41 magnesium alloy with the parameters indicated in the experimental section were cross-sectioned and analyzed by SEM (Figures 4 and 5). The high atomic number difference between the coating and the substrate makes that the coating appears in light contrast, while the substrate is in dark one.

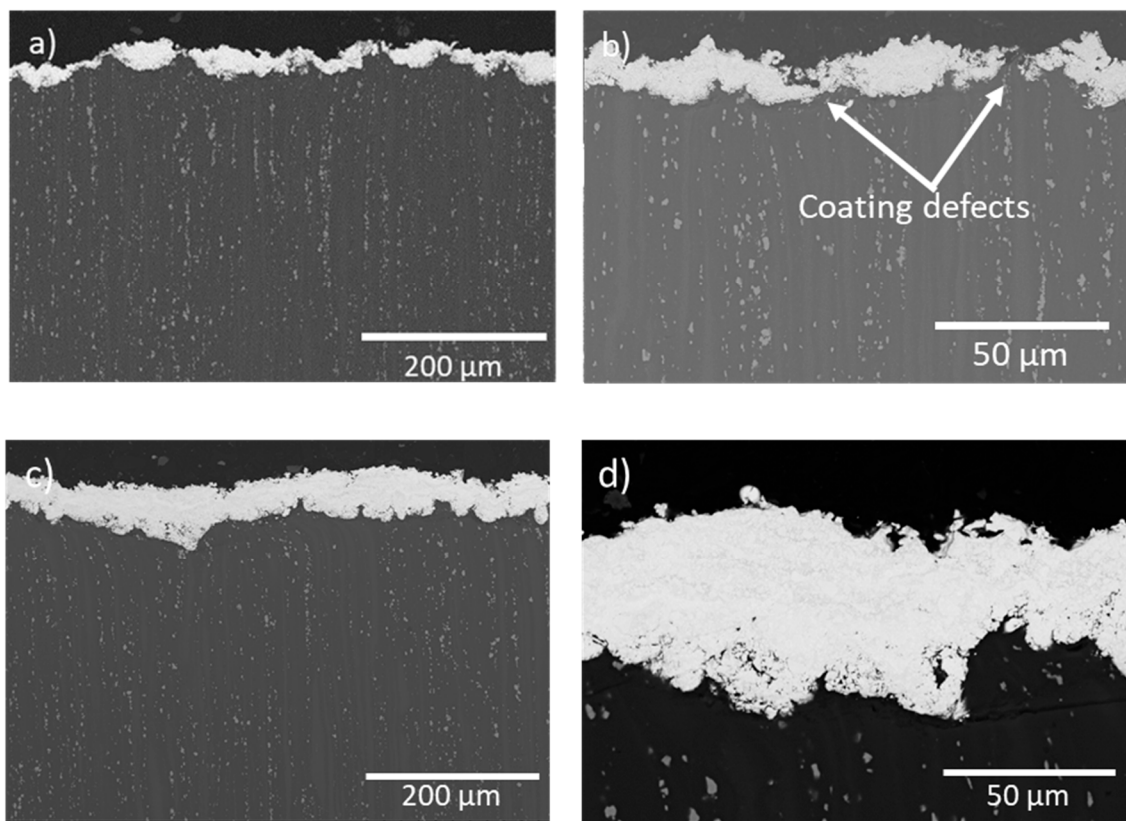


Figure 4. SEM micrographs of the cross section of (a) 1L-1 sample, (b) detailed view of 1L-1 coating, (c) 2L-1 sample and (d) detailed view of 2L-1 coating.

The one-layer coating (1L-1) (Figure 4a) coated the entire sample surface but it showed thickness variations and local defects (arrowed zones in Figure 4b) in which the substrate surface could be more exposed to the exterior. Also, in these zones, the presence of pores can be seen, while in the other zones of the coating, there are no visible pores. The average thickness of the WC-12Co layer deposited was $29.3 \pm 8.7 \mu\text{m}$ and its deposition caused a weight increase of $1.6 \times 10^{-2} \text{ g/cm}^2$ (Table 2). To put this data in context, this mass gain represents a 1% of the mass of the substrate and is equivalent to have a magnesium thickness increase of $85 \mu\text{m}$. Therefore, it is perfectly admissible for most engineering designs.

Table 2. Morphological features of the different coatings deposited.

Sample	Thickness (μm)	$\Delta m/\text{Area}$ (g/cm^2)	Porosity (%)	Roughness Ra (μm)	Adhesion (MPa)
1L-1	29.3 ± 8.7	1.6×10^{-2}	2.3 ± 1.4	4.3 ± 0.2	>50
2L-1	45.5 ± 6.7	4.0×10^{-2}	0.8 ± 0.2	4.9 ± 0.5	>50
2L-2	69.9 ± 9.8	7.7×10^{-2}	4.9 ± 1.6	4.4 ± 0.2	>50
2L-3	57.2 ± 14.2	6.7×10^{-2}	2.1 ± 0.5	4.4 ± 0.5	>50
2L-4	60.8 ± 9.1	7.4×10^{-2}	7.5 ± 1.3	4.9 ± 0.7	>50

The BSE micrograph of the cross-section of the two-layer WC-12Co coating deposited with the same spraying conditions (2L-1) is shown in Figure 4c. This coating was continuous, covered the entire surface of the magnesium alloy and it did not show local defects nor cracks. The coating only increased the system mass by $4.0 \times 10^{-2} \text{ g/cm}^2$.

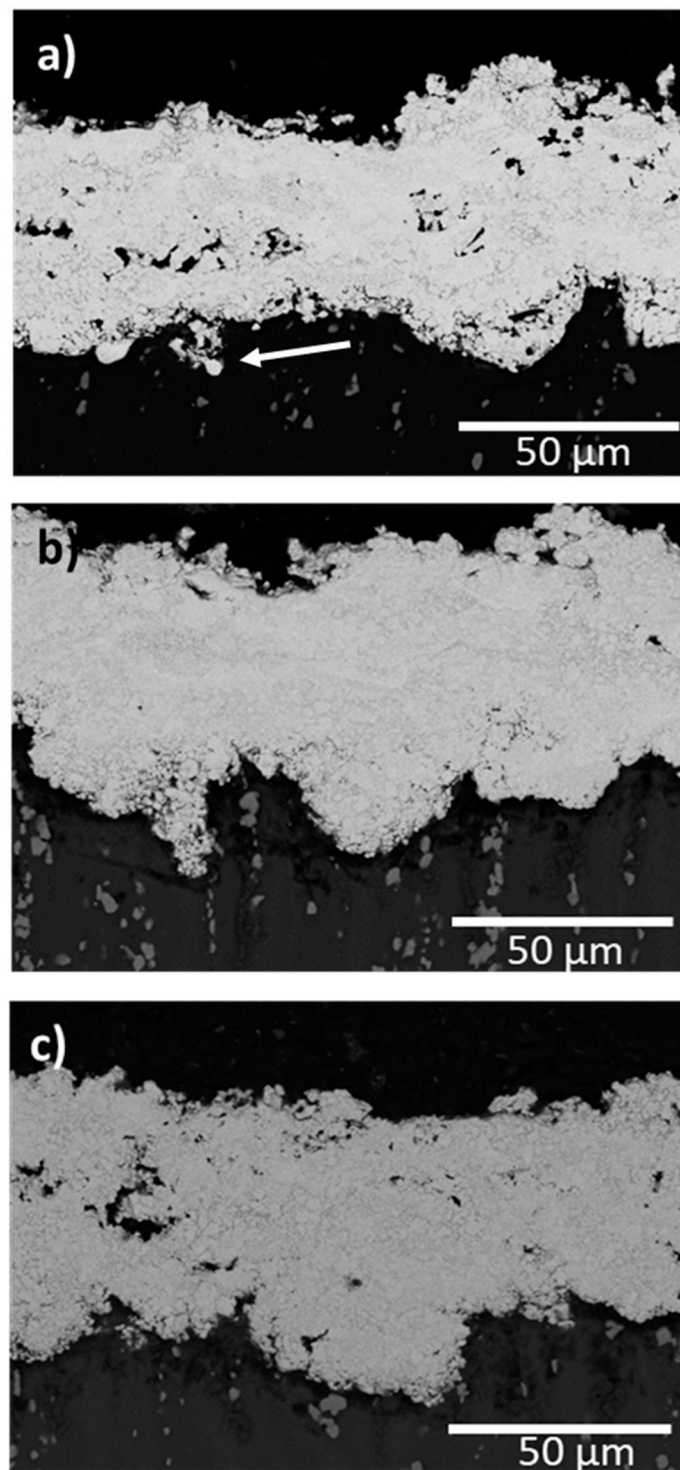


Figure 5. SEM micrographs of the cross section of (a) 2L-2, (b) 2L-3, and (c) 2L-4.

The coating thickness was $45.5 \pm 6.7 \mu\text{m}$ and there was no visible difference in the coating between the two sprayed layers, i.e., each individual layer cannot be distinguished (Figure 4d). The thickness is about 50% greater than the one-layer coating, but this can be explained by the continuity of the coating and by the compaction effect suffered by the first layer during the deposition of the second one. This explains that the porosity of the 2L-1 coatings was below 1 vol.%, while providing a continuous coating-substrate interface. Moreover, better deposition efficiency was obtained when the sprayed

particles reached the previously deposited WC-Co layer and it was still hot than when reaching the cold magnesium substrate.

Other two layers coatings were deposited by changing the gases mixture used. Figure 5 shows the cross section of 2L-2, 2L-3, and 2L-4 samples, being their O_2/H_2 ratio 0.34, 0.31, and 0.21, respectively, and with a nitrogen flow from 12.5 NLPM to 30.0 NLPM (used for particle transport). This was done in order to determine that the effect of an oxidizing or reducing atmosphere flame has on the composition and characteristics of the coatings, and the effect of a protective gas on the particles. In the cross section of the sprayed coatings it can be observed the high roughness effect causing by the impact of the particles on the magnesium substrate, which generates a penetration of the particles on the substrate of up to 20 μm . It can be also observed in some zones of the interface coating-magnesium substrate (marked by arrow in Figure 5a) the formation of a mixing zone for the coating and the substrate materials, as the mutual penetration of both materials into each other is produced [14].

Figure 5a shows the cross section of the 2L-2 sample. This coating had a thickness of $70 \pm 10 \mu m$ and caused a mass increase of $7.7 \times 10^{-2} g/cm^2$. It can be observed that the degree of porosity is higher than in the 2L-1 sample (Figure 5a), particularly in the middle of the coating, where the two layers should merge. The measured porosity value was 4.9% (Table 2), i.e., six times greater than with lower transport gas flow. It seems that the higher protective nitrogen flow (from 12.5 NLPM to 30.0 NLPM) has limited the temperature of the particles and, therefore, their ductility upon impacting with the substrate.

Figure 5b,c show the cross section of 2L-3 and 2L-4 samples which were sprayed with a reduced O_2/H_2 ratio. Both coatings had similar thickness (about 60 μm) and similar mass increase, $7 \times 10^{-2} g/cm^2$ in this case. No differences were observed in the main characteristics of these two coatings with the 2L-2 one, although the porosity reduced in the 2L-3 case. In this case, the atmosphere was slightly less oxidizing and, in the case of the 2L-3, the gases mixture was much less oxidizing. In all cases, the average surface roughness of all coatings was about 4.5 μm .

High adhesion strength values of all coatings to the substrate were obtained in the pull-off adhesion tests. The adhesive used in the tests cohesively failed without detaching the coatings from the substrate. For all coatings, average adhesion values higher than 50 MPa were obtained, this is the resistance of the adhesive and establishes an inferior limit of the coating adhesion. The substrate surface preparation by sand blasting and the high deformation level of the magnesium substrate because of the sprayed powder kinetic energy, observed in the previous SEM micrographs of the coatings, enhanced their mechanical adhesion.

3.3. Coatings Microstructure

Figure 6a shows the cross section of the 2L-1 coating at higher magnifications. The analysis of the different zones allows to observe different WC particles morphologies and also differences in the matrix contrast. In some zones the shape of the WC particles in the coating had geometrical shapes and were similar to those of the particles before spraying. However, in other zones, some particles had rounded edges what is indicative of dilution (Figure 6b). Also, the matrix around the rounded particles (arrow in Figure 6b) had a light contrast that indicates the presence of high mass atoms, suggesting that the dilution W in the Co matrix is taking place [40].

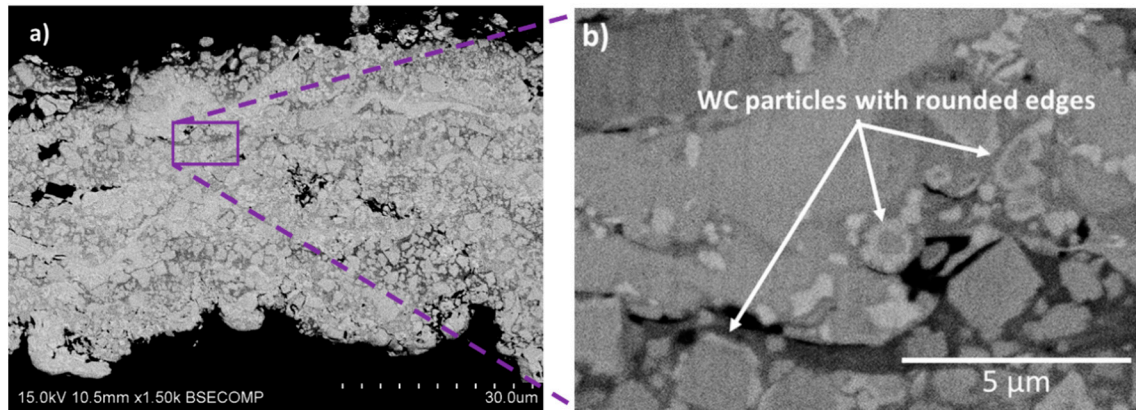


Figure 6. SEM micrographs in the cross-section of the two-layers WC-12Co coating: (a) general view and (b) details of the WC particles morphology in different coating zones.

In the SEM images, there were no substantial differences between the coatings deposited and only minor frequency of the rounded particles was observed in the coatings deposited with less oxidant flames.

To identify and quantify the different phases in the sprayed coatings, all coatings were analyzed by DRX (Figure 7). The peaks reveal the presence of the WC, W_2C , and W phases, being the WC and W_2C the major phases identified in all cases. In addition, a broad diffraction peak between 37° and 47° can be observed, and its presence is related with a presence of a quantity of amorphous or nanocrystalline material [27,41]. The intensity of the W_2C peaks in the 2L-1 spectrum is slightly greater than in the 1L-1 spectrum, and in the other two-layers coatings, which suggest a major degree of decarburization.

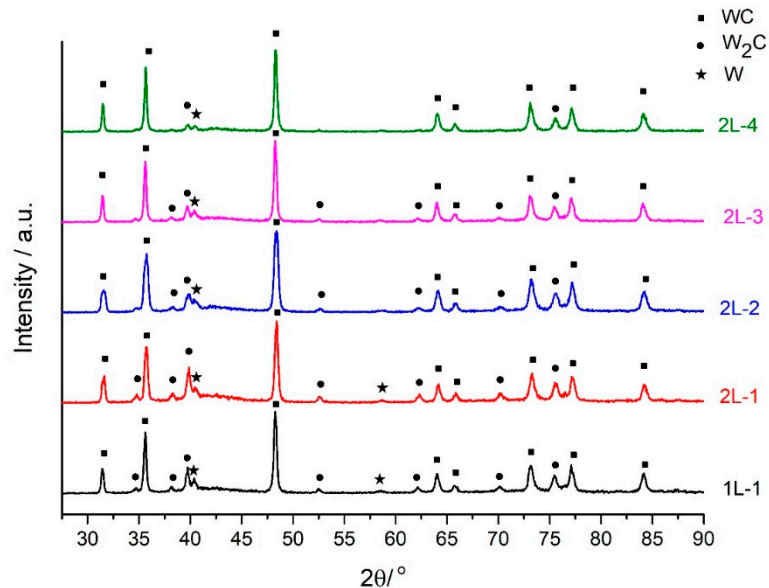


Figure 7. The X-ray diffraction measurements (DRX) diffraction patterns of 1L-1, 2L-1, 2L-2, 2L-3, and 2L-4 sprayed coatings.

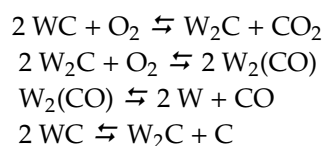
The different degree of decarburization can be compared using the “index of carbide retention, ICR” ($I_{ret.WC}$), defined by Bartuli et al. as [42] the relative intensities of the most intense peaks of the main phases:

$$I_{ret.WC} = \frac{I_{WC}}{(I_{WC} + I_{W_2C} + I_W)} \quad (2)$$

where the relative intensities of the most intense peaks of the WC, W₂C, and W phases are represented by I_{WC} , I_{W_2C} , and I_W , respectively.

The ICR values of the sprayed coatings were 0.65, 0.60, 0.70, 0.74, and 0.85 for 1L-1, 2L-1, 2L-2, 2L-3, and 2L-4, respectively. These results confirm the major degree of decarburization in the two layers coating using the highest O₂/H₂ ratio and the greatest gas transport flow. Moreover, when the coating was manufactured using the lowest O₂/H₂ ratio and the highest gas transport flow, as occurs in 2L-4, there is practically no decarburization. This is also related with the lower temperature of the particles in the flame as it was suggested by the morphology of the coatings.

The decarburization of the WC particles starts in-flight during the spraying process [40]. At elevated temperatures the mechanisms that control the process are the ones indicated below [43]:

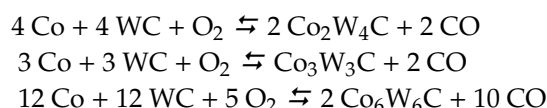


The mechanisms indicated show that in the presence of oxygen, WC is more prone to degradation, and also, that after diluting, W incorporates into Co intermetallic phases. This correlation is evidenced in Table 3, where it can be observed that the highest decarburization takes place in the most oxidant gases. Also, for equally oxidant atmospheres (samples 2L-1 and 2L-2), the reduction in the particle temperature explains the lower decarburization of the WC particles in 2L-2.

Table 3. Characteristics of the coatings deposited.

Sample	O ₂ /H ₂	Retained C (%)	Hardness (HV _{0.1})	Porosity (%)
1L-1	0.34	0.65	1400 ± 50	2.3 ± 1.4
2L-1	0.34	0.60	1380 ± 80	0.8 ± 0.2
2L-2	0.34	0.70	1230 ± 30	4.9 ± 1.6
2L-3	0.31	0.74	1230 ± 120	2.1 ± 0.5
2L-4	0.21	0.85	1050 ± 200	7.5 ± 1.3

Also, Co diffuses in the WC forming intermetallic phases through the following mechanisms [44]:



In our case, the DRX have identified the decarburization of WC but they have not detected the presence of the intermetallic phases. However, they have been observed by SEM in the shape of W rich phases (Figure 8) [45]. Also, the presence of dilution and formation of new phases with W in the Co phase is more frequent in the coatings that have lower porosity (Table 3). The intermetallic phase is formed at lower temperatures (600–800 °C) [46] and the phase distribution suggests that the wetting of the WC particles and of the Co matrix is high, so that the intermetallic phase filled the voids left by the hard particles, avoiding the formation of pores in the coatings.

Table 3 resumes the most relevant characteristics measured in the deposited coatings. Microhardness values measured in cross-section of the different samples were obtained. Values above 1050 HV were obtained, with values as high as 1380 HV and 1400 HV in the thinner coatings. These coatings show high hardness values, and are similar to the hardness values of bulk WC-Co material obtained by sintering [47] and of WC-Co deposited on high melting point substrates such as steel [34]. Hardness is higher in the coatings sprayed with the more oxidizing flame. This result can be explained as the combination of two opposite phenomena. On the one hand, the hardness of the coating depends on the hardness of the different phases involved, which should be higher in coatings that have retained more C. On the other hand, the presence of porosity is strongly reduced

by the presence of phases that have been formed as a result of the decarburization of the coating. Therefore, it seems that the presence of porosity is much more relevant than the differences observed in the composition of the coatings.

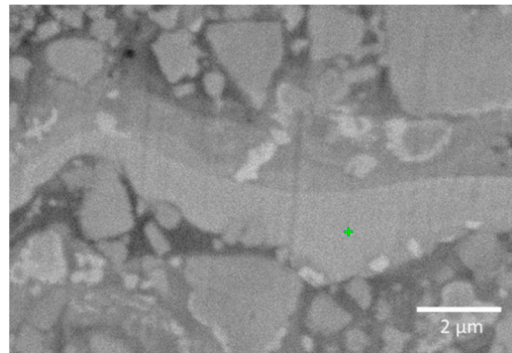


Figure 8. SEM micrograph in the cross-section of the two-layers WC-12Co coating where the presence of intermetallic phases can be observed.

One of the key points of this study was to deposit WC-Co coatings with high hardness values without damaging the substrates. Figure 9 shows that for the spraying distance used, no massive effects were observed in the samples, while using shorter spraying distances local deformation and even burning of the samples was observed. For the conditions used, only minor changes in the microstructure of the substrates were observed in the zone adjacent to the coating. 50 μm beneath the coating (arrowed in Figure 9), there was a partial dilution of the precipitates of the substrate and a refinement in the microstructure. Also, the modified zone of the magnesium substrate in its top 20 μm showed a 36% increase in hardness compared to the bulk. These effects indicate that the observed phenomena was not due to melting, but by plastic deformation induced by the WC-12Co particles during spraying that result in strain hardening of the substrate material [26,48].

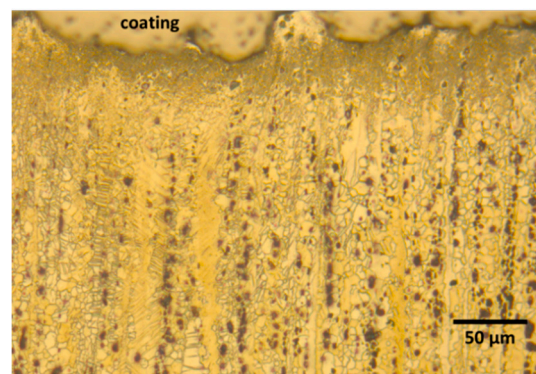


Figure 9. Optical micrograph of the interface ZE41-coating.

3.4. Tribological Results

Figure 10 shows optical macrographs and 3D optical profile micrographs of the wear tracks of the bare substrate and of the coated samples. There is a clear difference between the wear track obtained in the uncoated substrate (Figure 10a) and those of the coated specimens (Figure 10b–f) in terms of depth and width of the tracks. Wear track of the uncoated substrate was thick and deep, showing the low wear resistance of the ZE41 magnesium substrate. The main wear mechanisms observed in the ZE41 magnesium alloy were oxidation and abrasion, as has been reported before [26]. The average depth of the track obtained by 3D optical profiler was 510 μm and the width was 3800 μm .

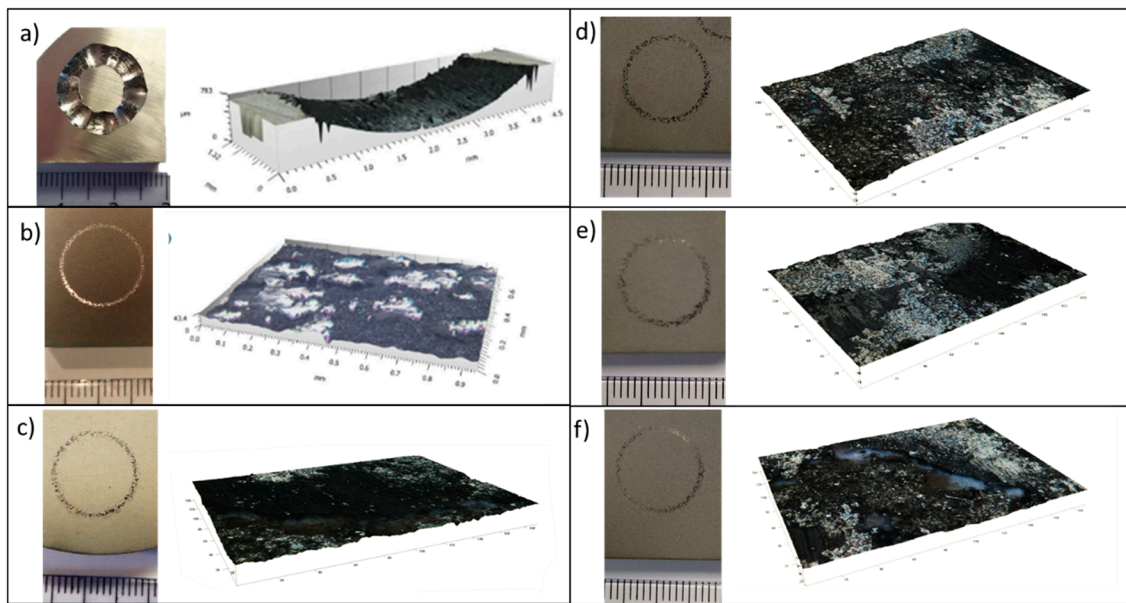


Figure 10. Optical macrographs and 3D optical profiler micrograph of the wear track of (a) ZE41 magnesium alloy, (b) 1L-1, (c) 2L-1, (d) 2L-2, (e) 2L-3, and (f) 2L-4.

The different coated systems effectively protected the substrate against wear after a sliding distance of 5000 m. The wear tracks observed (Figure 10b–d) in all the coated samples were very soft and only a change of the surface brightness denoted the presence of the wear test on the surface. For the one-layer coating (Figure 10b) metallic shine was observed in the wear track, which indicates that the coating was modified by the wear test and some uncoated zones were exposed to the environment. Despite this, the 3D optical profiler was not able to resolve the depth and width of this and of none of the other tracks of the coated systems.

The study of the tracks indicates that the roughness of the coating reduced in the contact zone, making the tracks brighter than the surrounding coating. However, apart from a modification equivalent to a polishing, no dimensional changes were observed in any of the systems studied. In the case of the one-layer coating, the path was less homogeneous than in other cases. This can be explained by the initial higher heterogeneity of the coating, and it indicates that the 5000 m wear test has not been capable of modifying it, even in the zones with defects.

The different wear parameters obtained after the test are shown Table 4. In all coated systems, the steady state friction coefficient obtained was 0.30. In the case of the bare magnesium substrate, the friction coefficient was 0.38 which is 26.6% greater than in the case of the coated specimens. The volumetric wear rate of the coated samples is 3 orders of magnitude smaller than the value obtained for the bare alloy (Table 4). This value further decreased by using a two layers system, being $8.3 \times 10^{-6} \text{ mm}^3/\text{m}$ for the one-layer coating and $2.6 \times 10^{-6} \text{ mm}^3/\text{m}$ for the 2L-1 coated sample. The volumetric wear rate obtained when changing the O_2/H_2 ratio (samples 2L-3 and 2L-4) was similar to that obtained for 2L-1 sample. However, the increase of the gas transport flow (sample 2L-2) resulted in the transference of material from the counterbody to the samples.

Table 4. Results summary of the tribological performance of each specimen.

Sample	Friction Coefficient	Wear Rate (mm ³ /m)
ZE41	0.38 ± 0.03	1.0 × 10 ^{−2}
1L-1	0.29 ± 0.02	8.3 × 10 ^{−6}
2L-1	0.29 ± 0.01	2.6 × 10 ^{−6}
2L-2	0.32 ± 0.03	−3.8 × 10 ^{−6}
2L-3	0.31 ± 0.02	1.3 × 10 ^{−6}
2L-4	0.27 ± 0.01	2.6 × 10 ^{−7}

A deeper analysis of the wear tracks of the coatings was made using SEM and a slight deterioration of the coatings was observed. Figure 11a,b show the surface wear tracks for the one-layer coating and two-layers coating, respectively. In both cases, and more visible at higher magnifications (Figure 11c,d), it can be observed that there are continuous bright zones and cracked darker ones.

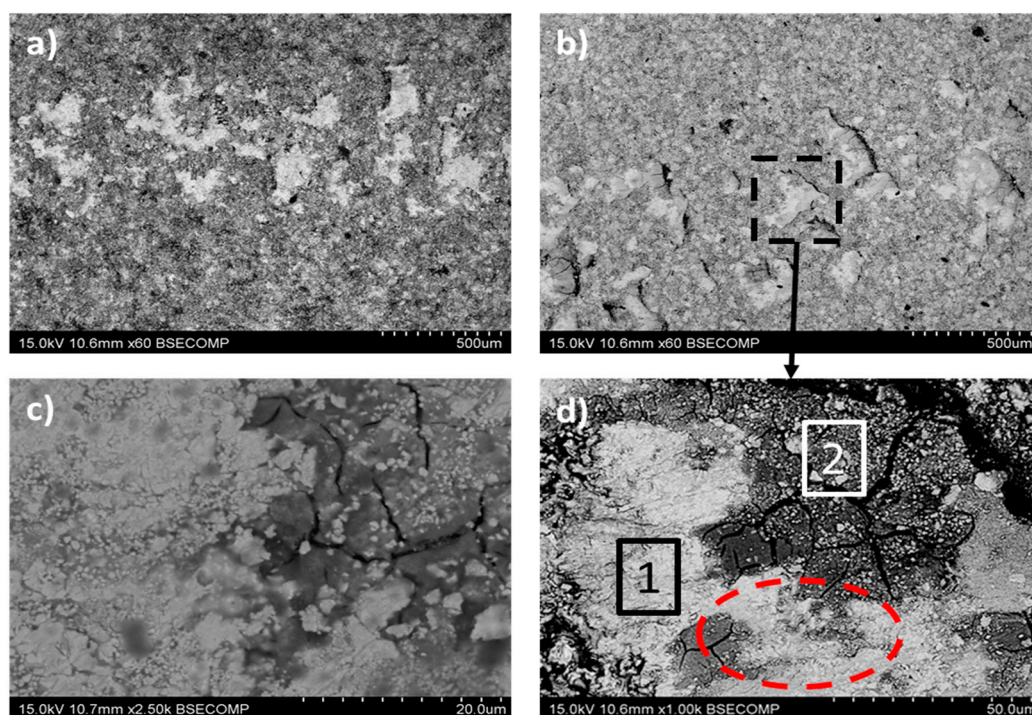


Figure 11. Backscattered SEM micrographs of the wear tracks of: (a) 1L-1 and (b) 2L-1. Higher magnifications of (c) 1L-1 and (d) 2L-1 coating.

EDX analysis, results are summarized in Table 5, showed that brighter zones (zone 1) are rich in W (78.6 wt.% of W), so that they correspond with the intermetallic precipitates formed during the spray and that have been identified as $\text{Co}_6\text{W}_6\text{C}$ and $\text{Co}_6\text{W}_4\text{C}$. In these zones, the amount of oxygen was very limited. On the other hand, the darker zones (zone 2) had about 30 wt.% of oxygen. This indicates the presence of a tribolayer, which is the result of the wear debris attachment during the dry sliding tests. This oxide zone is formed due to the high temperature reached at the sliding contact between the surface and the counterbody [18]. Some zones of the oxide layer were partially covered by the metallic part of the tribolayer (circled in Figure 11d) suggesting a higher ductility of this metallic part with respect to the oxidized one. Furthermore, some soft scratches are seen on this metallic zone (arrow marked in Figure 11d), revealing some contribution of abrasion mechanism in the wear of the sample.

Table 5. Chemical composition in wt.% of different zones of the wear track of the 2LWC coating.

Element	Zone 1 (wt.%)	Zone 2 (wt.%)
W	78.5	52.0
O	6.1	31.5
Co	10.4	4.5
C	5.0	11.9

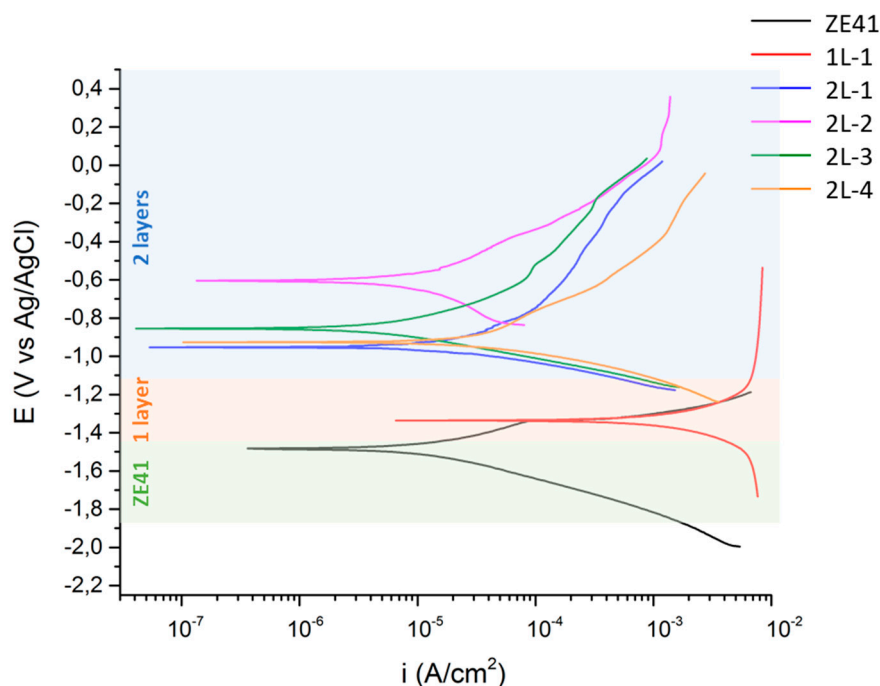
Therefore, wear in the coatings was the result of different wear mechanisms: (i) An initial wear stage in which the coating asperities are deformed and subsequently detached, forming the wear debris; (ii) ploughing for abrasion of the debris particles, and (iii) oxidative wear.

As a result of the wear tests it can be determined that the presence of high roughness values and defects in the one-layer coating was not a problem and that it protected the substrates from wear. It can be explained as a result of a combination of a very hard coating with small size defects in it, so the hardness avoids the contact of the deeper and uncoated zones with the counterbody even in the vicinity of the defects, and that this does not participate in the propagation of defects during wear. This makes that defects, so they do not contribute to the wear of the coating.

In any case, the use of these coatings provided up to 99% more wear resistance than uncoated ZE41 magnesium alloy.

3.5. Electrochemical Test

Figure 12 shows the anodic-cathodic polarization curves of the different coated systems and of the uncoated substrate after 1 h of immersion in 3.5 wt.% NaCl water solution at room temperature. The 1L-WC-1 coating only ennobled the potential to a value -1.3 V and it showed very high current densities for every potential, even greater than those of the uncoated substrate. The value of the 1L-WC-1 can be explained not only by means of the interaction between the saline solution and the substrate, but also by the formation of galvanic couples between the substrate and the metallic and intermetallic phases formed in the defective coating.

**Figure 12.** Anodic-cathodic polarization curves after 1 h immersion in NaCl 3.5 wt.% of the uncoated ZE41 magnesium alloy and the WC-Co-coated systems.

The two-layers coated samples showed increases in the corrosion potential of up to 0.9 V, from -1.493 V for the ZE41 magnesium alloy to -0.605 V for the 2L-2 coating. In these cases, there was no sign of interaction between the substrate and the solution and the values obtained seem to be only related with the interaction between the coating and the chloride media, showing a corrosion protection capability in these coatings. The differences in the values can be explained by means of the species that are formed in the coatings, particularly the presence of intermetallic precipitates in the 2L-2 may explain their high corrosion potential. In the other coatings, the retained carbide was higher than that and the presence of Co is more relevant. This makes that their corrosion potential is closer to the value of Co, which is ~ 1.0 V [49].

The analysis of the corrosion current density values reveals the different corrosion behavior of the tested specimens (Table 6). ZE41 magnesium alloy suffered a great corrosion attack in the first hour in contact with the electrolyte with a corrosion current density of $17.9 \mu\text{A}/\text{cm}^2$. The single layer coating increased the corrosion current density by two orders of magnitude with respect to the uncoated specimen to $1250.0 \mu\text{A}/\text{cm}^2$. As indicated before, the presence of defects in the coatings, the presence of metallic and intermetallic phases and diffusion across the coating accelerate the corrosion reactions due to the formation of galvanic couples that extend the corrosion process through all tested surface.

Table 6. Corrosion potential and current density obtained for the different specimens after 1 h of immersion in the electrolyte.

Sample	E_{corr} (V)	i_{corr} ($\mu\text{A}/\text{cm}^2$)
ZE41	-1.493	17.9
1L-1	-1.331	1250.0
2L-1	-0.950	7.3
2L-2	-0.605	8.6
2L-3	-0.852	3.9
2L-4	-0.922	22.1

The two-layers coatings 2L-1, 2L-2, and 2L-3 have a totally different corrosion response. They reduce the corrosion current density of the bare substrate by up to 78%, from $17.9 \mu\text{A}/\text{cm}^2$ to $3.9 \mu\text{A}/\text{cm}^2$ in the first hour, revealing a protective behavior against corrosion. The 2L-4 has similar corrosion current density than the magnesium alloy. This coating showed the highest porosity of the manufactured samples, and the presence of interconnected porosity in the coating would allow the electrolyte to reach the magnesium substrate and allow the corrosion of the substrate.

Figure 13 shows the general aspect of the different samples after 1 h of immersion in the electrolyte solution and after the electrochemical corrosion test. In the ZE41 magnesium surface a great corrosion attack can be observed in almost the whole exposed surface (dark zones in Figure 13a), and the release of corrosion products occurs. The surface of the 1L-1 specimen (Figure 13b) also revealed an extended corrosion attack. In this case, apart from the damage in the coating, many white corrosion products were formed on the surface. They consisted of magnesium hydroxide, $\text{Mg}(\text{OH})_2$, and indicate that corrosion is taking place in the magnesium substrate beneath the coating. In the two-layers coatings (Figure 13c–f) there was no significant attack in the surface and no magnesium corrosion products appeared. This indicates that these coatings were not degraded by the chloride solution and that the chloride solution did not reach the magnesium substrate.

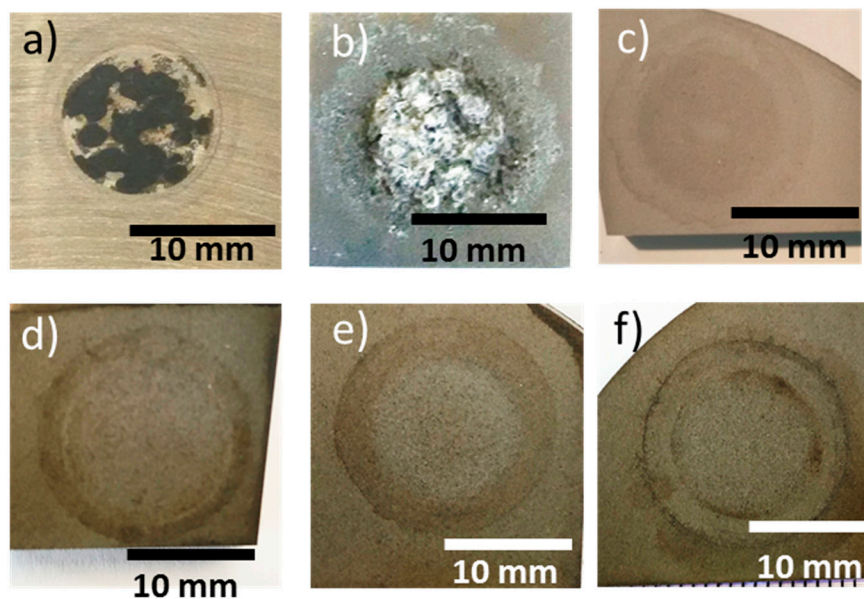


Figure 13. Plan view macrographs of the different coatings after the anodic-cathodic corrosion tests (scales in mm) (a) uncoated substrate and the different coated samples (b) 1L-1, (c) 2L-1, (d) 2L-2, (e) 2L-3, and (f) 2L-4.

The evolution of the R_p values of the different manufactured coatings and for the ZE41 magnesium alloy with time are shown in Figure 14a. Magnesium alloy and the 1L-1 coating system had the lowest R_p values for every testing time throughout the test. In both cases, a little increase of the polarization resistance with immersion time was observed. This can be attributed to the formation of a semi-protective oxide layer that slightly reduced the corrosive process, as it has already been observed by other authors for other magnesium alloys [18,50]. It is evident that a non-homogeneously one-layer coating promotes the corrosion of the substrate.

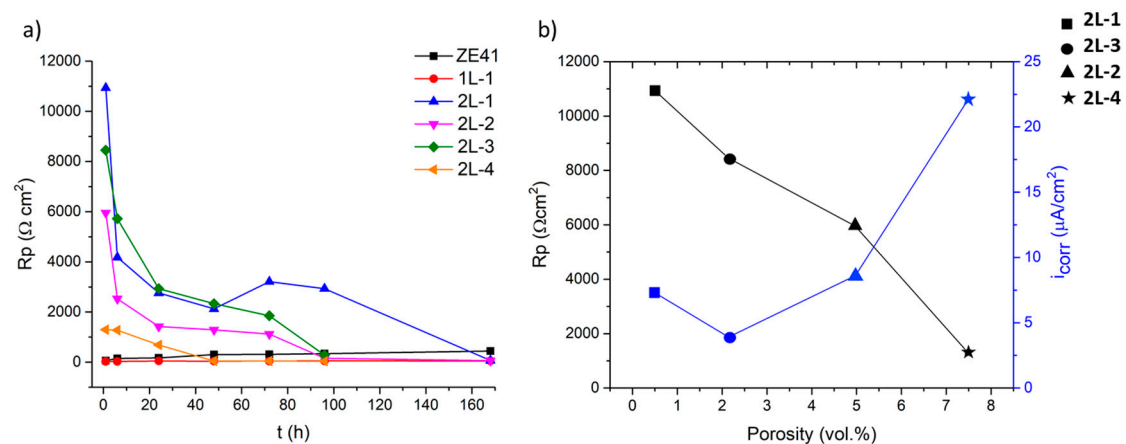


Figure 14. (a) Polarization resistance (R_p) values vs. immersion time in the NaCl 3.5 wt.% of the uncoated ZE41 magnesium alloy and the WC-Co coated systems. (b) Relation between R_p and i_{corr} values at 1h immersion with porosity degree for the different two-layers coated samples.

The different two-layers coatings had a high polarization resistance after 1 h of immersion. The value decreased after 6 h in contact with the electrolyte in all cases but, in any case, this value still was 40 times greater than the value of the uncoated specimen. At 1 h of immersion time, the highest R_p value was reached by 2L-1 sample (11,000 $\Omega \cdot \text{cm}^2$), which corresponds with the two-layers sample having the lowest degree of porosity. This value decreased with the increase of the immersion

time, but the corrosion protection of the coating slightly increased after 72 h in the electrolyte solution. This behavior can be associated to the formation of a corrosion products layer that protect the system and slightly decrease the corrosion process. After 72 h the value started to decrease because of the cracking of the corrosion products. After 168 h the value was similar than the uncoated magnesium substrate.

The R_p value of the two-layers coatings decreases with the increase of the porosity degree, while the i_{corr} values obtained increase with the increase of the porosity degree, as shown in Figure 14b. The presence of porosity, and, in some cases, of the interconnected porosity, allows the electrolyte to penetrate through the coating, reaching the magnesium substrate, producing its degradation, decreasing its polarization resistance (micro-crevice corrosion), and increasing its corrosion density. In all cases, the increase in the immersion time decreases the R_p value, until reaching the value obtained for the bare alloy after 168 h in the electrolyte solution.

At the lowest immersion times the most important parameter that affects the corrosion behavior is the compactness of the coating, but at longer times the corrosion attack starts due to the formation of galvanic couples at the surface of the coatings. As shown, the different spraying parameters used produce differences in the decarburization degree, showing the highest value of decarburization when using the highest O_2/H_2 ratio and the lowest gas transport flow (2L-1 sample). So, the top of the coatings is constituted by WC particles embedded in a Co matrix (with W and C), with different compositions. The dissimilar composition of the coating surface produces the formation of a galvanic cells between the Co matrix, that acts as an anode, and the WC particles, that act as a cathode, as well as with the presence of intermetallic precipitates and the Co matrix [40,51]. Thus, the decomposition of the WC particles and the consequent variation of the matrix composition produced during the spraying process makes its surface more vulnerable to the electrochemical attack and producing the final failure of the coating, as it occurs in 2L-1 and 2L-3 samples.

The optimal WC-12Co coating for the corrosion protection was obtained using spraying parameters of two layers, a O_2/H_2 ratio of 0.34 and a gas transport flow of 12.5 NLPM, because they minimize both the porosity and the decarburization degree.

4. Conclusions

WC-12Co coatings have been successfully deposited by HVOF on low melting ZE41 magnesium alloy. Only a partial dilution of the precipitates and a refinement of the microstructure in the substrate-coating interface were observed, showing an increase of 35.6% in their hardness compared to the bulk.

Thin coatings with thicknesses from 29 μm , for one-layer coating, to 70 μm for two-layers coatings were obtained. One-layer coating showed defects in the continuity of the coating while the two layers the coatings were continuous, covered the entire of the sprayed surface and had high adhesion to the substrate. The thickness of the coatings increased with the gas transport flow. The O_2/H_2 ratio used in the spraying process produced changes in the porosity of the coatings; the lowest amount was obtained using a ratio of 0.34.

WC, W_2C , and W intermetallic phases were observed in the coatings. The highest degree of decarburization was obtained for the two layers coating deposited using the highest O_2/H_2 ratio and the lowest gas transport flow. Decarburization was practically avoided when using the lowest O_2/H_2 ratio (0.21) and the highest gas transport flow (30 NLPM).

All deposited coatings provided wear resistance; wear rates of the coatings were 10^4 times smaller than for the magnesium substrate. The presence of defects in the one-layer coating did not have any effect on the behavior of the coatings.

All two-layers coated samples increased the corrosion potential of the ZE41 magnesium alloy and reduced their corrosion current density to a 22% of the uncoated one. Two-layers coating with the lowest degree of porosity effectively protected the substrate for at least 96 h in contact with 3 wt.% NaCl solution, reducing corrosion current density by one order of magnitude. In the other

coatings, the presence of porosity allowed the diffusion of chloride ions and corrosion took place in the coating-substrate interface.

Defects in the one-layer coating caused an increase of the corrosion rate because of the contact of the saline solution with the Mg substrate and the subsequent formation of galvanic couples. Therefore, this coating that is light and adequate for wear protection is not valid for the corrosion protection of magnesium substrates. The thickest and densest two-layers coatings provide both corrosion and wear protection to the magnesium substrate and demonstrates the validity of using HVOF as a low heat input.

Author Contributions: Investigation, S.G.-R. and V.B.; supervision, B.T. and J.R.; writing—original draft, S.G.-R.; writing—review and editing, A.J.L., B.T., and J.R. All authors have read and agreed the published version of the manuscript.

Funding: This research was funded by Ministerio de Economía, Industria y Competitividad grant number RTI2018-096391-B-C31 and Comunidad de Madrid project ADITIMAT-CM S2018/NMT-4411.

Acknowledgments: The authors wish to thank Ministerio de Economía, Industria y Competitividad (project RTI2018-096391-B-C31) and Comunidad de Madrid (Project ADITIMAT-CM S2018/NMT-4411) for funding.

Conflicts of Interest: The authors declare no conflict of interest.

References

1. Mehta, D.S.; Masood, S.H.; Song, W.Q. Investigation of wear properties of magnesium and aluminum alloys for automotive applications. *J. Mater. Process. Technol.* **2004**, *155*, 1526–1531. [\[CrossRef\]](#)
2. Mordike, B.L.; Ebert, T. Magnesium Properties-applications-potential. *Mater. Sci. Eng. A* **2001**, *302*, 37–45. [\[CrossRef\]](#)
3. Makar, G.L.; Kruger, J. Corrosion of magnesium. *Int. Mater. Rev.* **1993**, *38*, 138–153. [\[CrossRef\]](#)
4. Ardelean, H.; Frateur, I.; Zanna, S.; Atrous, A.; Marcus, P. Corrosion protection of AZ91 magnesium alloy by anodizing in niobium and zirconium-containing electrolytes. *Corros. Sci.* **2009**, *51*, 3030–3038. [\[CrossRef\]](#)
5. Chai, L.; Yu, X.; Yang, Z.; Wang, Y.; Okido, M. Anodizing of magnesium alloy AZ31 in alkaline solutions with silicate under continuous sparking. *Corros. Sci.* **2008**, *50*, 3274–3279. [\[CrossRef\]](#)
6. Pan, F.; Yang, X.; Zhang, D. Chemical nature of phytic acid conversion coating on AZ61 magnesium alloy. *Appl. Surf. Sci.* **2009**, *255*, 8363–8371. [\[CrossRef\]](#)
7. Torres, B.; Taltavull, C.; López, A.J.; Campo, M.; Rams, J. Al/SiCp and Al11Si/SiCp coatings on AZ91 magnesium alloy by HVOF. *Surf. Coat. Technol.* **2015**, *261*, 130–140. [\[CrossRef\]](#)
8. López, A.J.; Rams, J.; Ureña, A. Sol–gel coatings of low sintering temperature for corrosion protection of ZE41 magnesium alloy. *Surf. Coat. Technol.* **2011**, *205*, 4183–4191. [\[CrossRef\]](#)
9. Taltavull, C.; Torres, B.; Lopez, A.J.; Rodrigo, P.; Otero, E.; Atrous, A.; Rams, J. Corrosion behaviour of laser surface melted magnesium alloy AZ91D. *Mater. Des.* **2014**, *57*, 40–50. [\[CrossRef\]](#)
10. Hu, R.-G.; Zhang, S.; Bu, J.-F.; Lin, C.-J.; Song, G.-L. Recent progress in corrosion protection of magnesium alloys by organic coatings. *Prog. Org. Coat.* **2011**, *73*, 129–141. [\[CrossRef\]](#)
11. Zhong, C.; Liu, F.; Wu, Y.; Le, J.; Liu, L.; He, M.; Zhu, J.; Hu, W. Protective diffusion coatings on magnesium alloys: A review of recent developments. *J. Alloys Compd.* **2012**, *520*, 11–21. [\[CrossRef\]](#)
12. Gray, J.E.; Luan, B. Protective coatings on magnesium and its alloys—A critical review. *J. Alloys Compd.* **2002**, *336*, 88–113. [\[CrossRef\]](#)
13. Romanov, D.A.; Goncharova, E.N.; Budovskikh, E.A.; Gromov, V.E.; Ivanov, Y.F.; Teresov, A.D.; Kazimirov, S.A. Structure of electroexplosive TiC–Ni composite coatings on steel after electron-beam treatment. *Russ. Metall.* **2016**, *2016*, 1064–1071. [\[CrossRef\]](#)
14. Budovskikh, E.A.; Gromov, V.E.; Romanov, D.A. The formation mechanism providing high-adhesion properties of an electric-explosive coating on a metal basis. *Dokl. Phys.* **2013**, *58*, 82–84. [\[CrossRef\]](#)
15. Arrabal, R.; Pardo, A.; Merino, M.C.; Mohedano, M.; Casajús, P.; Merino, S. Al/SiC thermal spray coatings for corrosion protection of Mg–Al alloys in humid and saline environments. *Surf. Coat. Technol.* **2010**, *204*, 2767–2774. [\[CrossRef\]](#)

16. Kubatík, T.F.; Pala, Z.; Neufuss, K.; Vilémová, M.; Mušálek, R.; Stoulil, J.; Slepíčka, P.; Chráska, T. Metallurgical bond between magnesium AZ91 alloy and aluminium plasma sprayed coatings. *Surf. Coat. Technol.* **2015**, *282*, 163–170. [[CrossRef](#)]
17. Sidhu, T.S.; Agrawal, R.D.; Prakash, S. Hot corrosion of some superalloys and role of high-velocity oxy-fuel spray coatings-A review. *Surf. Coat. Technol.* **2005**, *198*, 441–446. [[CrossRef](#)]
18. Mandal, D.; Viswanathan, S. Effect of heat treatment on microstructure and interface of SiC particle reinforced 2124 Al matrix composite. *Mater. Charact.* **2013**, *85*, 73–81. [[CrossRef](#)]
19. Tao, Y.; Xiong, T.; Sun, C.; Kong, L.; Cui, X.; Li, T.; Song, G.-L. Microstructure and corrosion performance of a cold sprayed aluminium coating on AZ91D magnesium alloy. *Corros. Sci.* **2010**, *52*, 3191–3197. [[CrossRef](#)]
20. Spencer, K.; Fabijanic, D.M.; Zhang, M.-X. The use of Al–Al₂O₃ cold spray coatings to improve the surface properties of magnesium alloys. *Surf. Coat. Technol.* **2009**, *204*, 336–344. [[CrossRef](#)]
21. Campo, M.; Carboneras, M.; López, M.D.; Torres, B.; Rodrigo, P.; Otero, E.; Rams, J. Corrosion resistance of thermally sprayed Al and Al/SiC coatings on Mg. *Surf. Coat. Technol.* **2009**, *203*, 3224–3230. [[CrossRef](#)]
22. Taltavull, C.; Lopez, A.J.; Torres, B.; Atrens, A.; Rams, J. Optimisation of the high velocity oxygen fuel (HVOF) parameters to produce effective corrosion control coatings on AZ91 magnesium alloy. *Mater. Corros.* **2015**, *66*, 423–433. [[CrossRef](#)]
23. Tobergte, D.R.; Curtis, S. *Handbook of Thermal Spray Technology*; ASM International: Cleveland, OH, USA, 2013; Volume 53, ISBN 9788578110796.
24. García-Rodríguez, S.; Torres, B.; López, A.J.; Otero, E.; Rams, J. Characterization and mechanical properties of stainless steel coatings deposited by HVOF on ZE41 magnesium alloy. *Surf. Coat. Technol.* **2019**, *359*, 73–84. [[CrossRef](#)]
25. García-Rodríguez, S.; López, A.J.; Torres, B.; Rams, J. 316L stainless steel coatings on ZE41 magnesium alloy using HVOF thermal spray for corrosion protection. *Surf. Coat. Technol.* **2016**, *287*, 9–19. [[CrossRef](#)]
26. García-Rodríguez, S.; Torres, B.; Lopez, A.J.; Rainforth, W.M.; Otero, E.; Muñoz, M.; Rams, J. Wear Resistance of Stainless Steel Coatings on ZE41 Magnesium Alloy. *J. Therm. Spray Technol.* **2018**, *27*, 1615–1631. [[CrossRef](#)]
27. Stewart, D.A.; Shipway, P.H.; McCartney, D.G. Microstructural evolution in thermally sprayed WC-Co coatings: Comparison between nanocomposite and conventional starting powders. *Acta Mater.* **2000**, *48*, 1593–1604. [[CrossRef](#)]
28. Di Girolamo, E.S. Thermally sprayed nanostructured coatings for anti-wear and TBC applications: State-of-the-art and future perspectives. In *Anti-Abrasive Nanocoatings*; Woodhead Publishing: Cambridge, UK, 2015; pp. 513–541.
29. Han, J.C.; Jafari, M.; Park, C.G.; Seol, J.B. Microstructure-property relations in WC-Co coatings sprayed from combinatorial Ni-plated and nanostructured powders. *Mater. Charact.* **2017**. [[CrossRef](#)]
30. Hsiao, W.T.; Su, C.Y.; Huang, T.S.; Liao, W.H. Wear resistance and microstructural properties of Ni-Al/h-BN/WC-Co coatings deposited using plasma spraying. *Mater. Charact.* **2013**. [[CrossRef](#)]
31. Liu, Y.; Hang, Z.; Xi, N.; Chen, H.; Ma, C.; Wu, X. Erosion-Corrosion Behavior of HVOF WC-Co Coating in Cl[−] and SO₄^{2−} Containing Solutions. *Appl. Surf. Sci.* **2018**, *431*, 55–59. [[CrossRef](#)]
32. Matthews, S.J.; James, B.J.; Hyland, M.M. Microstructural influence on erosion behaviour of thermal spray coatings. *Mater. Charact.* **2007**, *58*, 59–64. [[CrossRef](#)]
33. Souza, V.A.D.; Neville, A. Corrosion and synergy in a WC-Co-Cr HVOF thermal spray coating-Understanding their role in erosion-corrosion degradation. *Wear* **2005**, *259*, 171–180. [[CrossRef](#)]
34. Wang, Q.; Chen, Z.H.; Ding, Z.X. Performance of abrasive wear of WC-12Co coatings sprayed by HVOF. *Tribol. Int.* **2009**, 1046–1051. [[CrossRef](#)]
35. Ma, N.; Guo, L.; Cheng, Z.; Wu, H.; Ye, F.; Zhang, K. Improvement on mechanical properties and wear resistance of HVOF sprayed WC-12Co coatings by optimizing feedstock structure. *Appl. Surf. Sci.* **2014**, 364–371. [[CrossRef](#)]
36. López, A.J.; Rams, J. Protection of carbon steel against molten aluminum attack and high temperature corrosion using high velocity oxygen-fuel WC-Co coatings. *Surf. Coat. Technol.* **2015**, *262*, 123–133. [[CrossRef](#)]
37. *Standard Test Method for Pull-Off Strength of Coatings Using Portable Adhesion Testers*; ASTM International: West Conshohocken, PA, USA, 2017; ASTM D4541.
38. *ISO Metallic Materials—Vickers Hardness Test—Part 1: Test Method*; International Organization for Standardization (ISO): Geneva, Switzerland, 2018; ISO 6507-1:2018.

39. Parco, M.; Zhao, L.; Zwick, J.; Bobzin, K.; Lugscheider, E. Investigation of HVOF spraying on magnesium alloys. *Surf. Coat. Technol.* **2006**, *201*, 3269–3274. [[CrossRef](#)]
40. Picas, J.A.; Rupérez, E.; Punset, M.; Forn, A. Influence of HVOF spraying parameters on the corrosion resistance of WC-CoCr coatings in strong acidic environment. *Surf. Coat. Technol.* **2013**, *225*, 47–57. [[CrossRef](#)]
41. Sudaprasert, T.; Shipway, P.H.; McCartney, D.G. Sliding wear behaviour of HVOF sprayed WC-Co coatings deposited with both gas-fuelled and liquid-fuelled systems. *Wear* **2003**, *255*, 943–949. [[CrossRef](#)]
42. Bartuli, C.; Valente, T.; Cipri, F.; Bemporad, E.; Tului, M. Parametric study of an HVOF process for the deposition of nanostructured WC-Co coatings. *J. Therm. Spray Technol.* **2005**, *14*, 187–195. [[CrossRef](#)]
43. Zhan, Q.; Yu, L.; Ye, F.; Xue, Q.; Li, H. Quantitative evaluation of the decarburization and microstructure evolution of WC-Co during plasma spraying. *Surf. Coat. Technol.* **2012**, *206*, 4068–4074. [[CrossRef](#)]
44. Lou, D.; Hellman, J.; Luhulima, D.; Liimatainen, J.; Lindroos, V.K. Interactions between tungsten carbide (WC) particulates and metal matrix in WC-reinforced composites. *Mater. Sci. Eng. A* **2003**, *340*, 155–162. [[CrossRef](#)]
45. Zhang, S.H.; Cho, T.Y.; Yoon, J.H.; Fang, W.; Song, K.O.; Li, M.X.; Joo, Y.K.; Lee, C.G. Characterization of microstructure and surface properties of hybrid coatings of WC-CoCr prepared by laser heat treatment and high velocity oxygen fuel spraying. *Mater. Charact.* **2008**, *59*, 1412–1418. [[CrossRef](#)]
46. Coddet, C. Thermal Spray: Meeting the Challenges of the 21st Century. In Proceedings of the 15th International Thermal Spray Conference, Nice, France, 25–29 May 1998; ASM International: Cleveland, OH, USA, 1998; p. 191.
47. Picas, J.A.; Xiong, Y.; Punset, M.; Ajdelsztajn, L.; Forn, A.; Schoenung, J.M. Microstructure and wear resistance of WC-Co by three consolidation processing techniques. *Int. J. Refract. Met. Hard Mater.* **2009**, *344*–349. [[CrossRef](#)]
48. Picas, J.A.; Menargues, S.; Martin, E.; Colominas, C.; Baile, M.T. Characterization of duplex coating system (HVOF + PVD) on light alloy substrates. *Surf. Coat. Technol.* **2017**, *318*, 326–331. [[CrossRef](#)]
49. Bodaghi, A.; Hosseini, J. Corrosion behavior of electrodeposited cobalt-tungsten alloy coatings in NaCl aqueous solution. *Int. J. Electrochem. Sci.* **2012**, *7*, 2584–2595.
50. Ahmadkhaniha, D.; Fedel, M.; Sohi, M.H.; Hanzaki, A.Z.; Deflorian, F. Corrosion behavior of magnesium and magnesium-hydroxyapatite composite fabricated by friction stir processing in Dulbecco's phosphate buffered saline. *Eval. Program Plann.* **2016**, *104*, 319–329. [[CrossRef](#)]
51. Lekatou, A.; Regoutas, E.; Karantzalis, A.E. Corrosion behaviour of cermet-based coatings with a bond coat in 0.5 M H₂SO₄. *Corros. Sci.* **2008**, *3389*–3400. [[CrossRef](#)]



© 2020 by the authors. Licensee MDPI, Basel, Switzerland. This article is an open access article distributed under the terms and conditions of the Creative Commons Attribution (CC BY) license (<http://creativecommons.org/licenses/by/4.0/>).